MDPI

Article

Honeycomb-like N-Doped Carbon Matrix-Encapsulated $Co_{1−x}S/Co(PO_3)_2$ Heterostructures for Advanced Lithium-Ion Capacitors

Yutao Liu [1], Xiaopeng Xie [2], Zhaojia Wu [2], Tao Wen [3], Fang Zhao [4], Hao He [3], Junfei Duan [3] and Wen Wang [5,*]

[1] International Institute of Engineering, Changsha University of Science and Technology, Changsha 410114, China; 19520009053@163.com

[2] Hunan Datang Xianyi Technology Co., Ltd., Changsha 410114, China; xnhqin@126.com (X.X.); win32logon@163.com (Z.W.)

[3] Materials Science and Engineering, Changsha University of Science and Technology, Changsha 410114, China; 19108471202@163.com (T.W.); hehao0520@gmail.com (H.H.); junfei_duan@csust.edu.cn (J.D.)

[4] Guangdong Power Grid Co., Ltd., Guangzhou Power Supply Bureau, Guangzhou 510660, China; 15603072389@163.com

[5] State Key Laboratory Disaster Prevention & Reduction for Power Grid, Changsha University of Science and Technology, Changsha 410114, China

* Correspondence: wew@csust.edu.cn

Abstract: Lithium-ion capacitors (LICs) are emerging as promising hybrid energy storage devices that combine the high energy densities of lithium-ion batteries (LIBs) with high power densities of supercapacitors (SCs). Nevertheless, the development of LICs is hindered by the kinetic imbalances between battery-type anodes and capacitor-type cathodes. To address this issue, honeycomb-like N-doped carbon matrices encapsulating $Co_{1−x}S/Co(PO_3)_2$ heterostructures were prepared using a simple chemical blowing-vulcanization process followed by phosphorylation treatment ($Co_{1−x}S/Co(PO_3)_2$@NC). The $Co_{1−x}S/Co(PO_3)_2$@NC features a unique heterostructure engineered within carbon honeycomb structures, which efficiently promotes charge transfer at the interfaces, alleviates the volume expansion of Co-based materials, and accelerates reaction kinetics. The optimal $Co_{1−x}S/Co(PO_3)_2$@NC composite demonstrates a stable reversible capacity of 371.8 mAh g^{-1} after 800 cycles at 1 A g^{-1}, and exhibits an excellent rate performance of 242.9 mAh g^{-1} even at 8 A g^{-1}, alongside enhanced pseudocapacitive behavior. The assembled $Co_{1−x}S/Co(PO_3)_2$@NC//AC LIC delivers a high energy density of 90.47 Wh kg^{-1} (at 26.28 W kg^{-1}), a high power density of 504.94 W kg^{-1} (at 38.31 Wh kg^{-1}), and a remarkable cyclic stablitiy of 86.3% retention after 5000 cycles. This research is expected to provide valuable insights into the design of conversion-type electrode materials for future energy storage applications.

Keywords: metal sulfides; anode material; heterostructures; honeycomb carbons; lithium-ion capacitors

1. Introduction

Lithium-ion capacitors (LICs) are considered promising candidates in the field of electrochemical energy storage due to their hybrid energy storage capabilities, which combine the high energy characteristics of lithium-ion batteries (LIBs) with the high power densities of supercapacitors (SCs). However, the practical implementation of LICs remains challenging due to the distinct energy storage mechanisms: the high-energy anodes operate through a slower, repeated Faraday reaction of lithium ions, while the cathodes undergo rapid anion absorption and desorption [1–3].

To address this challenge, researchers have devoted significant efforts to discovering new battery-type anode materials that offer both rapid rate performance and high capacities. Among these materials, cobalt sulfides, which are typical transition metal sulfides, show promise as conversion-type anodes due to their potential application on

account of their high theoretical specific capacities (590 mAh g^{-1}), weaker metal–sulfur bonds, and Co/Li$_2$S interfaces offering high electron transfer mobility [4,5]. However, cobalt sulfides experience significant volume expansion and contraction during repeated lithiation/delithiation cycles, leading to particles aggregation and the detrimental pulverization of electrode structures. This results in a rapid decline in rate performance, creating a mismatch with the capacitor-type cathodes in LICs. Numerous approaches have been proposed to improve reaction kinetics and structural stability, including downsizing particle size [6,7], constructing hierarchical porous structures [8,9], integrating with heteroatom-doped conductive carbonaceous materials [10–12], and fabricating heterogeneous architectures [13–15]. These approaches are expected to alleviate internal stress, increase contact with the electrolyte and shorten electronic and ionic transport pathways, enhance conductivity and maintain the integrity of the electrode materials, and regulate the electronic structure, ultimately aiming to enhance electrochemical performance, including increasing capacity, rate, and cycling stability. It is noteworthy that heterostructures composed of coupling components with large energy bandgap differences can induce a strong intrinsic electric field at the heterogeneous interfaces, thereby promoting reaction kinetics. Moreover, the as-formed heterointerfaces, characterized by abundant phase boundaries, have been shown to significantly influence rate capability and reversible capacity compared to individual components [16–18]. Recently, Dong and co-workers demonstrated that the CoS$_2$/Co$_4$S$_3$@NC heterogeneous composites exhibit high pseudocapacitive behavior and accelerate the diffusion rate of ions and electrons, thus improving the overall performance of the electrodes [19]. Wan and colleagues prepared a hierarchical binary metal sulfide (CoSn)S/C heterostructure, where the micro/nanostructures of (CoSn)S/C shorten the ion diffusion distance, facilitating the rapid transfer of Na$^+$ and enhancing the mechanical strength of the electrode [20]. Although cobalt-based sulfides play a significant role in improving the electrochemical properties of LICs, unlocking the potential of heterogeneous materials still requires a great deal of work to be explored.

Herein, honeycomb-like N-doped carbon matrices encapsulating Co$_{1-x}$S/Co(PO$_3$)$_2$ heterostructures are prepared using a simple chemical blowing-vulcanization process followed by phosphorylation treatment. The selection of Co$_{1-x}$S and Co(PO$_3$)$_2$ components is based on their bandgaps, which are 0 eV for Co$_{1-x}$S and approximately 2.6 eV for Co(PO$_3$)$_2$. The heterointerfaces between Co$_{1-x}$S and Co(PO$_3$)$_2$ components induce an internal electric field, increasing the number of electrochemical active sites, improving electrochemical kinetics, and stabilizing the structure during the repeated charge/discharge. Additionally, the integrated honeycomb-structured N-doped carbon matrices provide physical confinement to reduce nanograins aggregation, accommodate volume expansion during repeated long cycling, and ensure the integrity of the electrode materials, resulting in a high reversible capacity. As expected, the optimal Co$_{1-x}$S/Co(PO$_3$)$_2$@NC composite demonstrates a stable reversible capacity of 371.8 mAh g^{-1} after 800 cycles at 1 A g^{-1}, and an excellent rate performance of 242.9 mAh g^{-1} even at 8 A g^{-1}, accompanied with enhanced pseudocapacitive behavior. Furthermore, the assembled Co$_{1-x}$S/Co(PO$_3$)$_2$@NC//AC LIC delivers a high energy density of 90.47 Wh kg^{-1} (at 26.28 W kg^{-1}), a high power density of 504.94 W kg^{-1} (at 38.31 Wh kg^{-1}), and a high cyclic stability of 86.3% retention after 5000 cycles.

2. Results and Discussion

The synthetic strategy for the honeycomb-like N-doped carbon matrix decorated with Co$_{1-x}$S/Co(PO$_3$)$_2$ heterostructures is schematically illustrated in Figure 1a. Initially, polyvinylpyrrolidone (PVP), serving as the carbon source, weakly coordinates with Co^{2+} to form a sol–gel coordination complex precursor [21,22]. The precursor provides physical confinement to prevent the agglomeration of Co$_{1-x}$S nanograins during the calcination process. Subsequently, the precursor and mixed sulfur powder undergo thermal blowing-vulcanization treatment. Due to the high viscosity of molten PVP, the pyrolysis gasses (NO$_2$, NO, etc.) released from nitrate ions generate numerous bubbles as the temperature rises. These bubbles rapidly rupture, promoting the growth of interconnected thin carbon

walls, resulting in the formation of N-doped carbon matrices decorated with cobalt sulfides that resemble a 3D honeycomb-like structure. Afterwards, $Co_{1-x}S/Co(PO_3)_2$@NC is obtained through a facile phosphorylation process of the $Co_{1-x}S/$@NC composite, yielding conformal $Co_{1-x}S/Co(PO_3)_2$ heterostructures. FESEM results from Figure 1b–d show that the as-prepared $Co(PO_3)_2$@NC, $Co_{1-x}S$@NC, and $Co_{1-x}S/Co(PO_3)_2$@NC composites exhibit a typical 3D interconnected honeycomb-like framework comprising numerous thin carbon walls with smooth surfaces. This indicates sulfides/phosphides are uniformly encapsulated within the carbon matrices. This structure facilitates electrolyte penetration and effectively mitigates the volume change in active species during repeated cycling, thereby maintaining structural stability. TEM was employed to further examine the morphology and chemical properties. As shown in Figures 1e–g and S1–S3, numerous small nanoparticles are found within the carbon matrices of all the $Co_{1-x}S/Co(PO_3)_2$@NC, $Co_{1-x}S$@NC, and $Co(PO_3)_2$@NC composites. Notably, the $Co_{1-x}S/Co(PO_3)_2$@NC contains nanoparticles with an average size of less than 5 nm, demonstrating shortened electronic and ionic transport paths and effectively relieving internal strain during the electrochemical process. The lattice spacings of 0.268 and 0.254 nm in the higher magnification image (Figure 1e,f) correspond to the (130) plane of $Co(PO_3)_2$ and the (101) plane of $Co_{1-x}S$, respectively. Similarly, the lattice spacings of 0.194 and 0.187 nm in Figure 1g correspond to the (102) plane of $Co_{1-x}S$ and the (−242) plane of $Co(PO_3)_2$, respectively, confirming the successful fabrication of heterostructures. The energy dispersive X-ray spectrometer (EDS) spectrum in Figure 1h confirmed the uniform dispersion of Co, S, P, N, and O in the carbon matrices.
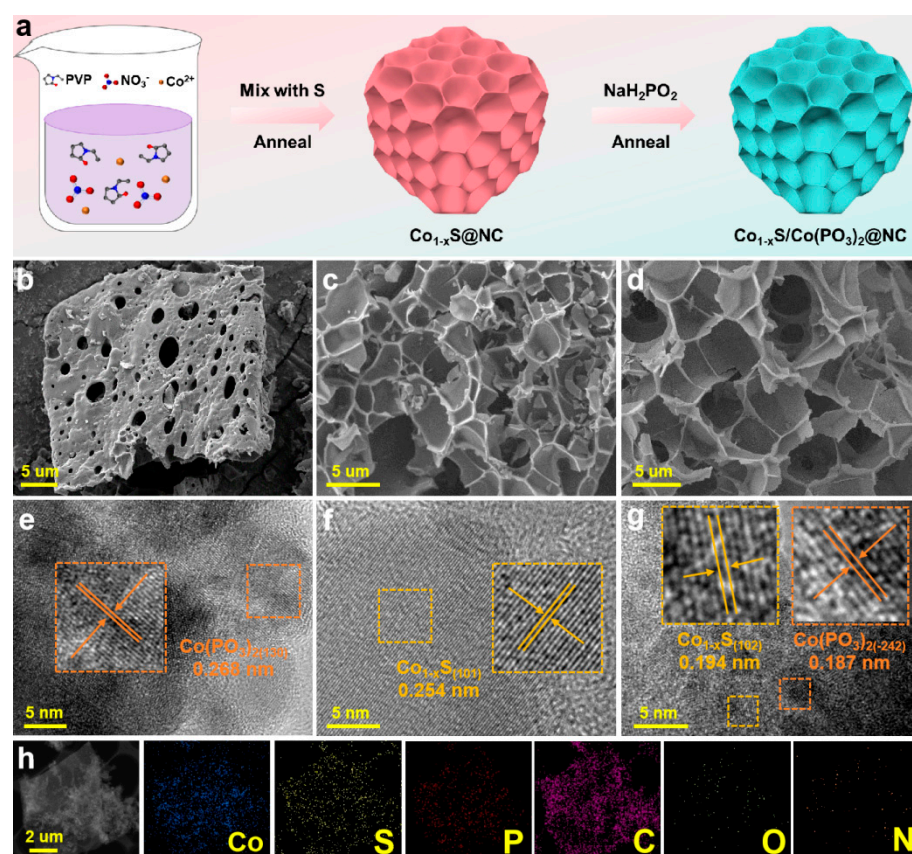

Figure 1. (**a**) Schematic illustration of synthetic process. SEM images of (**b**) $Co(PO_3)_2$@NC, (**c**) $Co_{1-x}S$@NC, and (**d**) $Co_{1-x}S/Co(PO_3)_2$@NC. HRTEM images of (**e**) $Co(PO_3)_2$@NC, (**f**) $Co_{1-x}S$@NC, and (**g**) $Co_{1-x}S/Co(PO_3)_2$@NC. (**h**) Elemental mapping of $Co_{1-x}S/Co(PO_3)_2$@NC.

The crystal structure of the synthesized materials was characterized using X-ray diffraction (XRD) patterns, as depicted in Figure 2a. The diffraction peaks of the $Co_{1-x}S/Co(PO_3)_2$@NC composites were consistently indexed to the monoclinic $Co(PO_3)_2$ phase (JCPDS No. 27-

1120) and the hexagonal $Co_{1-x}S$ phase (JCPDS No. 42-0826). For the $Co_{1-x}S@NC$ and $Co(PO_3)_2@NC$ composites, only single phases of $Co_{1-x}S$ and $Co(PO_3)_2$ were observed, without any impurity peaks. Moreover, the Raman spectra for three samples (Figure 2b) exhibit two prominent peaks at ~1351 and ~1371 cm^{-1}, which represent the graphitic carbon (G-band) and disordered carbon (D-band), respectively. This confirms the presence of N-doped carbon matrices. The relatively larger intensity ratio of I_D/I_G for $Co_{1-x}S/Co(PO_3)_2@NC$ (0.989) implies a higher degree of structural defects compared to $Co_{1-x}S@NC$ (0.973) and $Co(PO_3)_2@NC$ (0.969), which is conducive for fast electron transfer [23]. Thermogravimetric analysis (TGA) was conducted to determine the contents of $Co_{1-x}S$, $Co(PO_3)_2$, and carbon in $Co_{1-x}S/Co(PO_3)_2@NC$ (Figure 2c). As reported in our previous work, $Co_{1-x}S$ undergoes a multi-stage reaction involving complex oxidation processes in the air followed by carbon combustion [24,25]. The evaporation of adsorbed water accounts for the slight mass loss in the range of 50–200 °C. The oxidation of $Co_{1-x}S$ to $CoSO_4$ and Co_3O_4 is the primary cause of a notable weight loss, as well as the combustion of NC, as the temperature increases from 200 to 650 °C. Notably, the differences between the curves of $Co_{1-x}S/Co(PO_3)_2@NC$ and $Co_{1-x}S@NC$ are primarily attributed to the greater weight loss from NC combustions compared to the increase from oxidation of $Co_{1-x}S$. The TGA curves indicate the percentages of $Co_{1-x}S$, $Co(PO_3)_2$, and NC in $Co_{1-x}S/Co(PO_3)_2@NC$, which were 40.9 wt%, 29.4 wt%, and 29.7 wt%, respectively.
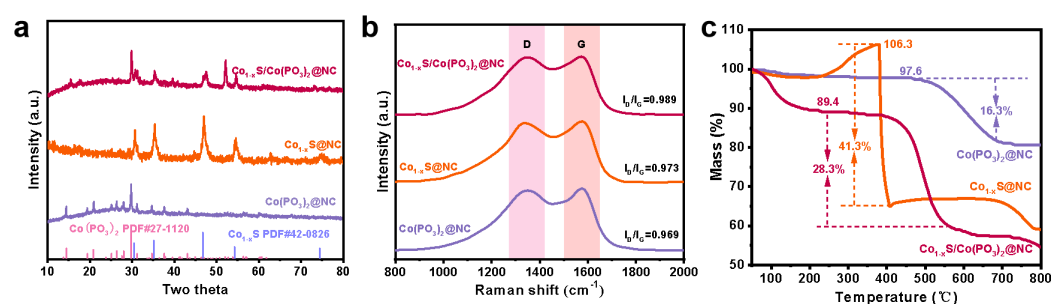
Figure 2. (**a**) XRD patterns, (**b**) Raman spectra, and (**c**) TGA curvesof $Co(PO_3)_2@NC$, $Co_{1-x}S@NC$, and $Co_{1-x}S/Co(PO_3)_2@NC$, respectively.

Furthermore, the surface chemical compositions of the three samples were analyzed using X-ray photoelectron spectroscopy (XPS) measurements. As shown in Figure 3a, elements such as cobalt, sulfur, phosphorus, oxygen, carbon, and nitrogen were clearly detected. The Co 2p high-resolution spectra, presented in Figure 3b, reveal the characteristic peaks at ~798.4 eV and ~782.6 eV, corresponding to Co $2p_{1/2}$ and Co $2p_{3/2}$ of Co^{2+}, along with their satellite peaks [26,27]. An additional set of peaks in the $Co_{1-x}S@NC$ composites, located at ~793.4 eV and 778.4 eV, is associated with Co^0 and suggests that the vulcanization process of the $PVP-Co^{2+}$ precursors is not fully completed. Figure 3c shows the S 2p spectra, where characteristic peaks at approximately 165.2 eV and 164.0 eV are associated with S $2p_{1/2}$ and S $2p_{3/2}$ of the C-S-C bond, while peaks at ~162.9 eV and ~161.8 eV correspond to S $2p_{1/2}$ and S $2p_{3/2}$ of S^{2-} [28]. Additionally, a peak at ~168.5 eV corresponds to SO_x likely due to inevitable surface oxidation. The strong chemical bonds between active species and carbon substrate are indicated by the presence of C-S-C, ensuring robust structures and excellent cycling stability during the intercalation and de-intercalation of Li^+ [29]. The characteristic peak at ~134.4 eV (Figure 3d) corresponds to P-O bonds. The C 1s peaks can be deconvoluted into three distinct peaks at ~284.8, ~285.9, and ~289.0 eV (Figure 3e), corresponding to C-C, C-N/C-O/C-S, and C=O bonds, respectively. The successful nitrogen substitution in the carbon matrix is confirmed by the presence of the C-N bond, and this is supported by the N 1s high-resolution spectra (Figure 3f). The nitrogen dopant can not only enhance interfacial wettability, create more defects and active sites, and accelerate reaction kinetics [30].
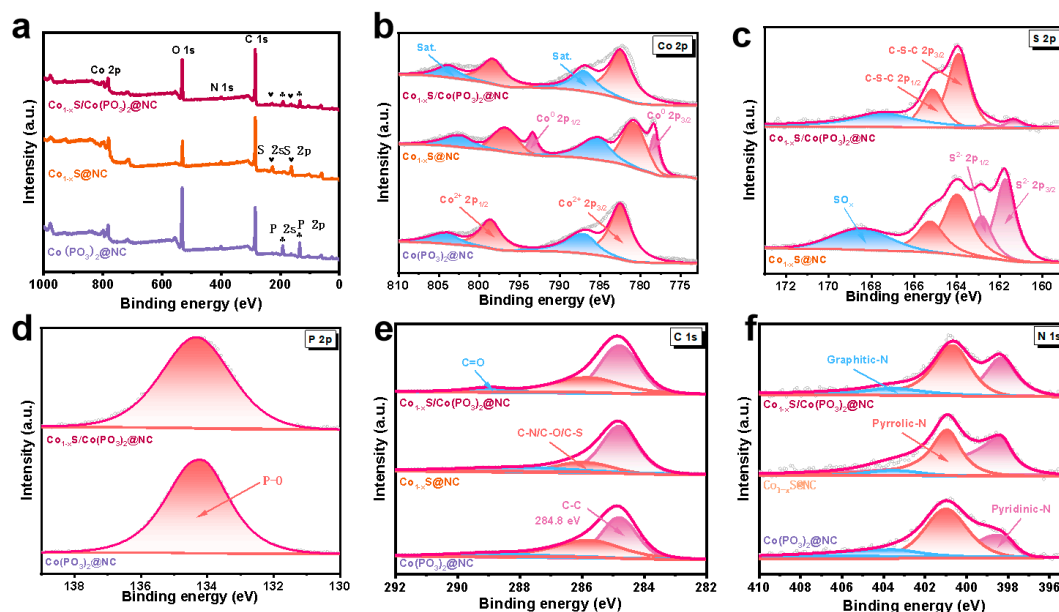
Figure 3. (**a**) The wide scan XPS of $Co(PO_3)_2$@NC, $Co_{1-x}S$@NC, and $Co_{1-x}S/Co(PO_3)_2$@NC, (**b**) Co 2p of $Co(PO_3)_2$@NC, $Co_{1-x}S$@NC, and $Co_{1-x}S/Co(PO_3)_2$@NC, (**c**) S 2p and (**d**) P 2p of $Co_{1-x}S$@NC and $Co_{1-x}S/Co(PO_3)_2$@NC, (**e**) C 1s and (**f**) N 1s of $Co_{1-x}S$@NC and $Co_{1-x}S/Co(PO_3)_2$@NC.

The Li^+ storage behavior of the $Co_{1-x}S/Co(PO_3)_2$@NC electrodes was evaluated using lithium metal as a counter electrode in an assembled 2032 coin-type half-cell. First, as shown in Figure 4a, cyclic voltammetry (CV) curves were measured at a sacn rate of 0.2 mV s^{-1}, revealing the electrochemical process over the first five cycles. In the initial cathodic scan, the sample showed significant broad peaks ~0.52 V and ~0.94 V, indicative of irreversible transformations and the formation of a solid electrolyte interface (SEI). In the subsequent scans, a set of new characteristic cathodic peaks appeared at 1.98 and 1.24 V related to the stepwise conversion reaction of $Co_{1-x}S$ into Co/Li_2S, $Co(PO_3)_2$ to CoP_2/Li_2O intermediates, and Co/Li_3P products; additionally, notable oxidation peaks were observed at 1.32, 2.05, and 2.56 V, corresponding to the oxidation reactions of Co/Li_2S to $Co_{1-x}S$ and Co/Li_3P to CoP_2 [31], which persisted in the following scans. The galvanostatic charge/discharge (GCD) profiles of the $Co_{1-x}S/Co(PO_3)_2$@NC electrode displayed initial charge/discharge capacities of $1194.0/719.1$ mAh g^{-1} with an initial Coulombic efficiency of 60.2%; in subsequent cycles, the capacities remained stable over 200 cycles with Coulombic efficiency, approaching to 99.6% (Figure 4b). The cycling performance reveals that the $Co_{1-x}S/Co(PO_3)_2$@NC electrode maintains the highest reversible capacity of 643.7 mAh g^{-1} after 200 cycles at 0.2 A g^{-1}, significantly exceeding those of $Co_{1-x}S$@NC (336.5 mAh g^{-1}), $Co(PO_3)_2$@NC (274.0 mAh g^{-1}) (Figure 4c), $Co_{1-x}S/Co(PO_3)_2$@NC-1v3 (478.4 mAh g^{-1}), and $Co_{1-x}S/Co(PO_3)_2$@NC-1v8 (426.8 mAh g^{-1}) (Figure S4). The rate capability of all samples was further examined across different current densities ranging from 0.2 to 8.0 A g^{-1}. The $Co_{1-x}S/Co(PO_3)_2$@NC exhibited the best rate performance regardless of current density, with a high capacity of 642.7 mAh g^{-1} at 0.2 A g^{-1} and 242.9 mAh g^{-1} at 8.0 A g^{-1} (Figure 4d,e); the rate performance of $Co_{1-x}S/Co(PO_3)_2$@NC is superior to some previously reported cobalt sulfide-based anode materials (Figure 4f). The long-term cycling performance of $Co_{1-x}S/Co(PO_3)_2$@NC, $Co_{1-x}S$@NC, and $Co(PO_3)_2$@NC electrodes was further compared at a current density of 1 A g^{-1}. As shown in Figures 4g and S4, the $Co_{1-x}S/Co(PO_3)_2$@NC electrode delivers an obvious higher reversible capacity and improved cycling stability (371.8 mAh g^{-1} after 800 cycles), while $Co(PO_3)_2$@NC maintains a capacity of only 230.1 mAh g^{-1}, which is lower than the reversible capacity for $Co_{1-x}S/Co(PO_3)_2$@NC-1v3 and $Co_{1-x}S/Co(PO_3)_2$@NC-1v8. This difference in performance is mainly due to the synergistic effect of the heterogeneous interface and the integrated honeycomb-structured carbon, which efficiently promote charge transfer at

the interfaces and accelerate the reaction kinetics, accommodate volume changes during prolonged long cycling, and ensure the structural integrity of the electrode materials.
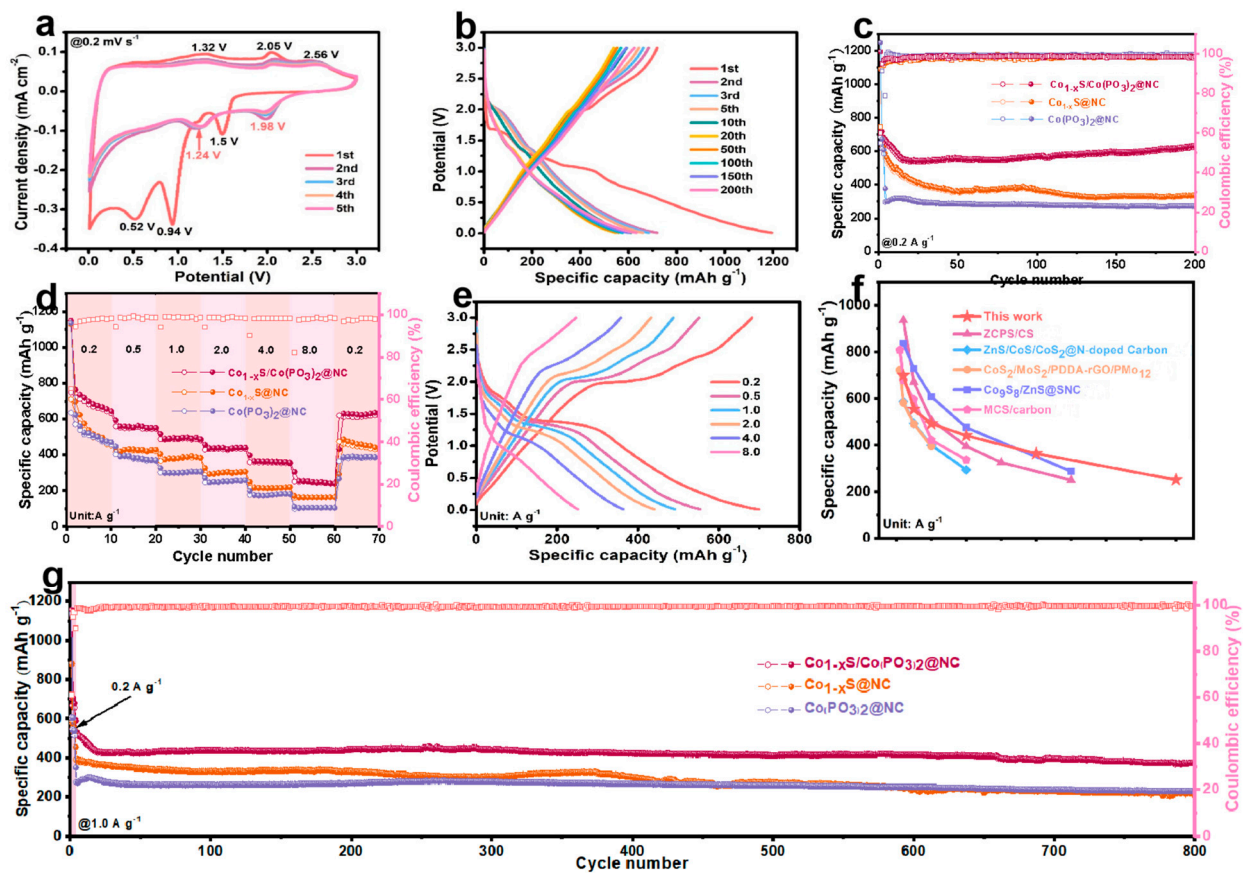

Figure 4. (**a**) The initial three CV curves of $Co_{1-x}S/Co(PO_3)_2$@NC at 0.2 mV s^{-1}, (**b**) galvanostatic charge/discharge profiles of $Co_{1-x}S/Co(PO_3)_2$@NC at 0.2 A g^{-1}, (**c**) cycling stability and coulombic efficiency at 0.2 A g^{-1} for 200 cycles, (**d**,**e**) rate capability and galvanostatic charge/discharge profiles of three samples, (**f**) corresponding comparison with reported studies, (**g**) long-term performance at 1.0 A g^{-1} for 800 cycles [32–36].

In order to assess the superior lithium storage capabilities of the $Co_{1-x}S/Co(PO_3)_2$@NC, cyclic voltammetry (CV) curves were recorded at various scanning rates, ranging from 0.1 to 5.0 mV S^{-1} (Figure 5a). As the scan rate increased, there were no discernible changes in the number or peak voltage of the observed peaks in the CV curves, indicating that $Co_{1-x}S/Co(PO_3)_2$@NC has good reversibility. It is widely accepted that the following Equation (1) could be used to explain the relationship between peak current (*i*) and scan rate (*v*):

$$i = av^b \tag{1}$$

where both *a* and *b* are variable parameters. The value of *b* can be used to diagnose whether the reaction is a diffusion-controlled reaction (for *b* = 0.5) or surface-controlled (for *b* = 1.0). As shown in Figure 5b, the *b* values at the *O1* peak and *R1* peak of the $Co_{1-x}S/Co(PO_3)_2$@NC electrodes were determined to be 0.66 and 0.67, respectively, suggesting a combination of diffusion-controlled and capacitive-controlled behaviors. Furthermore, the proportion of pseudocapacitive contribution could be quantified using the following Equation (2),

$$i = k_1v + k_2v^{1/2} \tag{2}$$

where k_1v and $k_2v^{1/2}$ indicate the current response from the capacitive capacity and diffusion-controlled capacity, respectively. As shown in Figure 5c,d, the pseudocapacitive

contributions of the $Co_{1-x}S/Co(PO_3)_2$@NC electrodes at the scanning rate of 2.0 mV s^{-1} were evaluated to be 70.0%. With the increase in v, the pseudocapacitive contribution gradually increases from 52.3% to 74.7%, demonstrating the important effect of the heterostructure in facilitating the electrode reaction kinetics. Figure 5e shows the Nyquist plots of three samples after three cycles at 0.1 A g^{-1}. All EIS spectra display similar characteristics, including two sections: a semicircular region at a medium- to high-frequency corresponding to R_{ct} and a linear region at low-frequency associated with Li$^+$ diffusion. Compared to $Co(PO_3)_2$@NC and $Co_{1-x}S$@NC, the $Co_{1-x}S/Co(PO_3)_2$@NC electrode exhibits significantly smaller R_{ct} in the medium- to high-frequency range (186 Ω compared to 304 Ω, 201 Ω), indicating that the unique heterostructures and effective particle refinement indeed enhance charge transfer and reaction kinetics. Moreover, based on the following equations related to diffusion coefficient of Li$^+$:
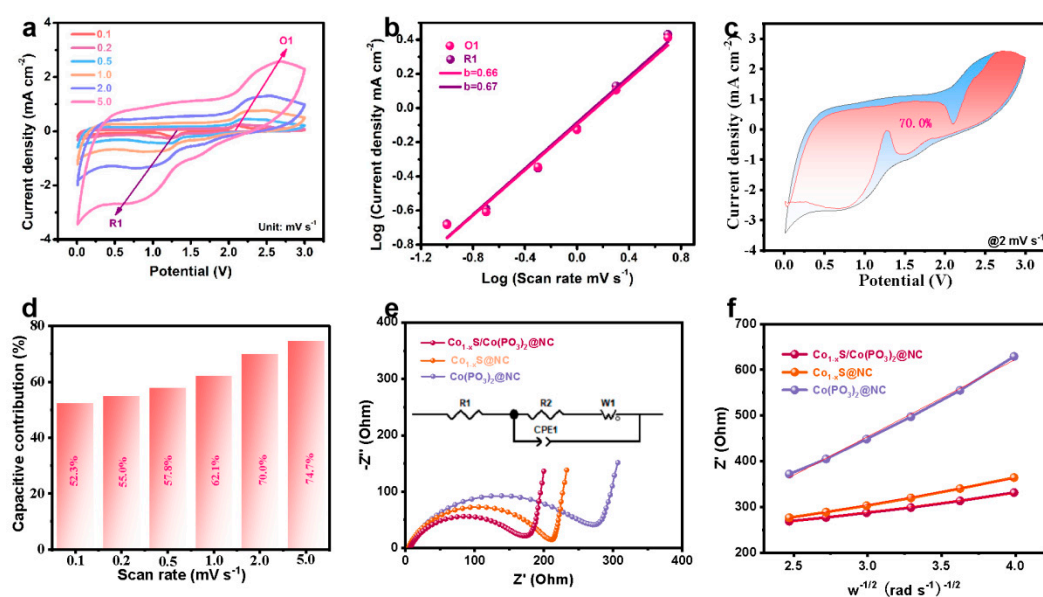
$$Z' = R_s + R_{ct} + \sigma\omega^{-1/2} \tag{3}$$

Figure 5. (**a**) CV curves at different sweep rates, (**b**) linear plot of Log *v*-Log *i*, (**c,d**) pseudocapacitive contribution of the $Co_{1-x}S/Co(PO_3)_2$@NC electrode at 2.0 mV s^{-1} and at different sweep rates, (**e,f**) Nyquist plots and the Z' as a function of $\omega^{-1/2}$ of of $Co(PO_3)_2$@NC, $Co_{1-x}S$@NC and $Co_{1-x}S/Co(PO_3)_2$@NC.

According to Equation (3), the Warburg factor (σ) of the two electrodes was calculated based on the linear relationship between Z' and $\omega^{-1/2}$ (Figure 5f). The value of σ for the $Co_{1-x}S/Co(PO_3)_2$@NC electrode (41.0) is much lower than the $Co_{1-x}S$@NC (57.6) and $Co(PO_3)_2$@NC electrodes (168.9). As the D_{Li+} diffusion coefficient is inversely proportional to the square of the Warburg factor (σ) [3], this lower σ value indicates a faster Li$^+$ diffusion coefficient for the $Co_{1-x}S/Co(PO_3)_2$@NC electrode.

Considering the exceptional electrochemical performance of the $Co_{1-x}S/Co(PO_3)_2$@NC in half-cells, a prelithiated $Co_{1-x}S/Co(PO_3)_2$@NC anode and an AC cathode were combined in an optimal mass ratio of 2:1 to assemble a $Co_{1-x}S/Co(PO_3)_2$@NC@NC//AC LIC device. This device was subsequently evaluated for its electrochemical energy storage properties within a voltage window of 0–4.0 V. The working principle of the assembled LIC is illustrated in Figure 6a. During charging, Li$^+$ ions either intercalate into $Co_{1-x}S/Co(PO_3)_2$@NC or adsorb onto the anode surface, while PF$_6^-$ anions are absorbed onto the AC surface. The discharge process reverses these actions. Figure 6b presents the CV curves of the LICs at scan rates of 5, 10, 20, 30, and 50 mV s^{-1}. Even at 50 mV s^{-1}, a rectangular profile is observed, indicating the capacitive behavior of the LICs [37,38]. The rate

performance of the LICs was assessed under various current densities, revealing reversible capacities of 19.15 mAh g^{-1} even at 2 A g^{-1}, respectively (Figure 6c,d). The assembled optimal Co$_{1-x}$S/Co(PO$_3$)$_2$@NC//AC LIC delivers a high energy density of 90.47 Wh kg^{-1} (at 26.28 W kg^{-1}) and a high power density of 504.94 W kg^{-1} (at 38.31 Wh kg^{-1}). Furthermore, Figure 6e illustrates the long-term cycling stability of the LICs, showing a high cyclic stability of 86.3% retention after 5000 cycles at a current of 2 A g^{-1}, accompanied by a Coulombic efficiency close to 100%. The superiorities of the as-prepared Co$_{1-x}$S/Co(PO$_3$)$_2$ heterostructures were compared with the reported literature in terms of synthetic methods and electrochemical performance (Table S1). In practical applications, the LICs successfully power a light-emitting diode (LED) to illuminate a "wang" character, further demonstrating the potential of the Co$_{1-x}$S/Co(PO$_3$)$_2$ heterostructures as an electrode material for Li-ion capacitors.
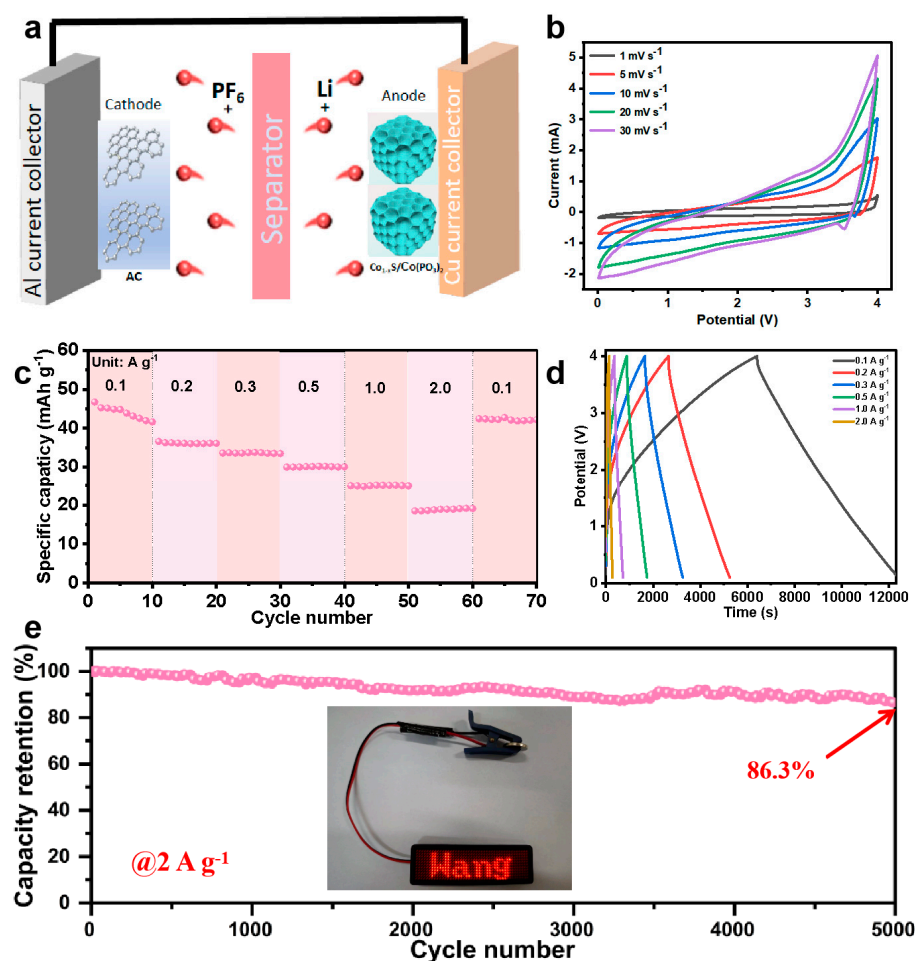

Figure 6. (**a**) Schematic illustration of the assembled Co$_{1-x}$S/Co(PO$_3$)$_2$@NC//AC LICs, (**b**) CV curves, (**c**) galvanostatic charge/discharge profiles, (**d**) rate capability, (**e**) long-term durability at 2 A/g of Co$_{1-x}$S/Co(PO$_3$)$_2$@NC//AC LICs.

3. Conclusions

In summary, we have constructed high-performance LICs using Co$_{1-x}$S/Co(PO$_3$)$_2$@NC as the anode material. This material is synthesized through the chemical blowing-vulcanization of a Co^{2+}-PVP precursor followed by phosphorylation treatment. The characteristic heterointerface and 3D honeycomb-like N-doped carbon matrix efficiently boost interfacial charge dynamics, provide spatial confinement for refined particles, and prevent structural degradation during repeated charge/discharge cycles. As a result, the optimal Co$_{1-x}$S/Co(PO$_3$)$_2$@NC composite demonstrates a stable reversible capacity of 371.8 mAh g^{-1} after 800 cycles at 1 A g^{-1}, showcasing significant pseudocapacitive contributions. The

assembled $Co_{1-x}S/Co(PO_3)_2@NC//AC$ LIC delivers a power density of 504.94 W kg^{-1} and an energy density of 90.47 Wh kg^{-1} within the voltage range of 0–4.0 V. Moreover, they exhibit a high cyclic stability of 86.3% retention after 5000 cycles at 2 A g^{-1}. The facile synthetic method opens new avenues for the fabrication of cost-effective, advanced energy storage devices utilizing Co-based sulfides heterostructures with balanced performance.

Supplementary Materials: The following supporting information can be downloaded at https://www.mdpi.com/article/10.3390/batteries10100346/s1: Figure S1: SEM image of $Co(PO_3)_2@NC$ composites; Figure S2: SEM image of $Co_{1-x}S@NC$ composites; Figure S3: SEM image of $Co_{1-x}S/Co(PO_3)_2@NC$ composites; Figure S4: (a) cycling performance at 0.2 A g^{-1}, (b) rate capability, (c) long-term performance at 1.0 A g^{-1} of $Co_{1-x}S/Co(PO_3)_2@NC$, $Co_{1-x}S/Co(PO_3)_2@NC$-1v3, and $Co_{1-x}S/Co(PO_3)_2@NC$-1v8 electrodes; Table S1: The LICs performance comparison among Co1-xS/Co(PO3)2@NC and other materials [39–46].

Author Contributions: Conceptualization, J.D. and W.W.; methodology, Y.L. and X.X.; validation, T.W. and H.H.; investigation, Z.W. and F.Z.; writing—original draft preparation, Y.L., X.X. and T.W.; writing—review and editing, Y.L., Z.W. and T.W.; visualization, Y.L. and W.W.; supervision, J.D. and W.W. All authors have read and agreed to the published version of the manuscript.

Data Availability Statement: The data that supported the findings of this study are available from the corresponding author upon reasonable request.

Conflicts of Interest: Authors Xiaopeng Xie and Zhaojia Wu were employed by the company Hunan Datang Xianyi Technology Co., Ltd. Author Fang Zhao was employed by the company Guangdong Power Grid Co., Ltd., Guangzhou Power Supply Bureau. The remaining authors declare that the research was conducted in the absence of any commercial or financial relationships that could be construed as a potential conflict of interest.

References

1. Sun, J.L.; Luo, B.C.; Li, H.X. A Review on the Conventional Capacitors, Supercapacitors, and Emerging Hybrid Ion Capacitors: Past, Present, and Future. *Adv. Energy Sustain. Res.* **2022**, *3*, 2000216–2100191. [CrossRef]
2. Liang, J.; Wang, D.W. Design rationale and device configuration of lithium-ion capacitors. *Adv. Energy Mater.* **2022**, *12*, 2200920. [CrossRef]
3. Wang, L.; Zhang, X.; Li, C.; Sun, X.Z.; Wang, K.W.; Su, F.Y.; Liu, F.Y.; Ma, Y.W. Recent advances in transition metal chalcogenides for lithium-ion capacitors. *Rare Met.* **2022**, *41*, 2971–2984. [CrossRef]
4. Yan, T.; Hu, H.; Duan, J.; Zhu, C.; Wang, Y.; Wen, J.; Li, L.; Xu, Z.; Wen, T.; Yang, P.; et al. Achieving superior sodium storage performance of sulfide heterostructures via copper-driven and electrochemical reconstruction strategy. *Chem. Eng. J.* **2024**, *499*, 155871. [CrossRef]
5. Liang, L.P.; Li, J.C.; Zhu, M.Y.; Li, Y.; Chou, S.L.; Li, W.X. Cobalt Chalcogenides/Cobalt Phosphides/Cobaltates with Hierarchical Nanostructures for Anode Materials of Lithium-Ion Batteries: Improving the Lithiation Environment. *Small* **2021**, *17*, 1903418. [CrossRef]
6. Liu, X.; Zhang, K.; Lei, K.X.; Li, F.J.; Tao, Z.L.; Chen, J. Facile synthesis and electrochemical sodium storage of CoS_2 micro/nano-structures. *Nano Res.* **2016**, *9*, 198–206. [CrossRef]
7. Wang, X.; Chen, Y.; Fang, Y.J.; Zhang, J.T.; Gao, S.Y.; Lou, X.W. Synthesis of cobalt sulfide multi-shelled nanoboxes with precisely controlled two to five shells for sodium-ion batteries. *Angew. Chem. Int. Ed.* **2019**, *58*, 2675–2679. [CrossRef]
8. Xiao, Y.; Hwang, J.Y.; Belharouak, I.; Sun, Y.K. Superior Li/Na-storage capability of a carbon-free hierarchical CoSx hollow nanostructure. *Nano Energy* **2017**, *32*, 320–328. [CrossRef]
9. Zheng, Y.Y.; He, L.; Kong, X.R.; Song, Y.; Zhao, Y. Three-dimensional porous N-doped graphite carbon with embedded CoS_2 nanoparticles as advanced anode for sodium-ion batteries. *Appl. Surf. Sci.* **2022**, *603*, 154481. [CrossRef]
10. Wang, L.; Zhang, X.; Kong, Y.Y.; Li, C.; An, Y.B.; Sun, X.Z.; Wang, K.; Ma, Y.W. Metal-organic framework-derived CoSe₂@ N-doped carbon nanocubes for high-performance lithium-ion capacitors. *Rare Met.* **2024**, *43*, 2150–2160. [CrossRef]
11. Li, Q.; Jiao, Q.Z.; Yan, Y.; Li, H.J.; Zhou, W.; Gu, T.T.; Shen, X.R.; Lu, C.X.; Zhao, Y.; Zhang, Y.Y.; et al. Optimized Co-S bonds energy and confinement effect of hollow MXene@CoS_2/NC for enhanced sodium storage kinetics and stability. *Chem. Eng. J.* **2022**, *450*, 137922. [CrossRef]
12. Lei, D.; Gao, Y.; Hou, Z.; Ren, L.; Jiang, M.; Cao, Y.; Zhang, Y.; Wang, J.-G. A Superior Lithium-Ion Capacitor Based on Ultrafine MnO/Dual N-Doped Carbon Anode and Porous Carbon Cathode. *Batteries* **2023**, *9*, 241. [CrossRef]

13. Lin, Y.; Qiu, Z.; Li, D.; Ullah, S.; Hai, Y.; Xin, H.; Liao, W.; Yang, B.; Fan, H.; Xu, J.; et al. NiS_2@CoS_2 nanocrystals encapsulated in N-doped carbon nanocubes for high performance lithium/sodium ion batteries. *Energy Storage Mater.* **2018**, *11*, 67–74. [CrossRef]

14. Liu, J.; Xu, Y.G.; Kong, L.B. Cleverly embedded CoS_2/NiS_2 on two-dimensional graphene nanosheets as high-performance anode material for improved sodium ion batteries and sodium ion capacitors. *J. Mater. Sci. Mater. Electron.* **2020**, *31*, 9946–9959. [CrossRef]

15. Wang, L.; Zhao, S.S.; Zhang, X.; Xu, Y.N.; An, Y.B.; Li, C.; Yi, S.; Liu, C.; Wang, K.; Sun, X.Z.; et al. In Situ Construction of Bimetallic Selenides Heterogeneous Interface on Oxidation-Stable $Ti_3C_2T_x$ MXene Toward Lithium Storage with Ultrafast Charge Transfer Kinetics. *Small* **2024**, 2403078. [CrossRef] [PubMed]

16. Xue, F.F.; Fan, F.F.; Zhu, Z.C.; Zhang, Z.G.; Gu, Y.F.; Li, Q.H. MoS_2/CoS heterostructures grown on carbon cloth as free-standing anodes for high-performance sodium-ion batteries. *Nanoscale* **2023**, *15*, 6822–6829. [CrossRef]

17. Cai, J.M.; Zhou, Y.L.; Tao, S.S.; Liu, Y.C.; Deng, W.T.; Hou, H.H.; Zou, G.Q.; Ji, X.B. Nanocrystalline Heterostructure with Low Voltage Hysteresis for Ultrahigh-Power Sodium-Ion Capacitors. *Energy Storage Mater.* **2024**, *71*, 103582. [CrossRef]

18. Xiao, Y.H.; Kong, Y.; Wang, X.Z.; Luo, H.R.; Yuan, G.Z.; Zhang, S.W.; Zhang, A.Q.; Zhou, J.; Fan, Y.Y.; Xin, L.; et al. Synergetic interface engineering and space-confined effect in $CoSe_2$@$Ti_3C_2T_x$ heterostructure for high power and long life sodium ion capacitors. *J. Colloid Interface Sci.* **2025**, *677*, 577–586. [CrossRef]

19. Dong, C.F.; Guo, L.J.; Li, H.B.; Zhang, B.; Gao, X.; Tian, F.; Qian, Y.T.; Wang, D.B.; Xu, L.Q. Rational fabrication of CoS_2/Co_4S_3@N-doped carbon microspheres as excellent cycling performance anode for half/full sodium ion batteries. *Energy Storage Mater.* **2020**, *25*, 679–686. [CrossRef]

20. Wan, S.Y.; Cheng, M.; Chen, H.Y.; Zhu, H.J.; Liu, Q.M. Nanoconfined bimetallic sulfides (CoSn)S heterostructure in carbon microsphere as a high-performance anode for half/full sodium-ion batteries. *J. Colloid Interface Sci.* **2022**, *609*, 403–413. [CrossRef]

21. Zhao, M.T.; Lu, Q.P.; Ma, Q.L.; Zhang, H. Two-Dimensional Metal-Organic Framework Nanosheets. *Small Methods* **2017**, *1*, 1600030. [CrossRef]

22. Yang, M.; Yan, Z.H.; Zhang, H.; Li, J.W.; Zhu, Z.Q.; Liu, L.; Jiao, L.F. Controllable Synthesis of Sub-10 nm ZnS Nanograins Confined in Micro-Size Carbon Skeleton for Aqueous Zn-S Batteries. *Adv. Funct. Mater.* **2024**, 2406077–2406085. [CrossRef]

23. Wen, F.; Zhu, C.; Li, L.; Zeng, G.; Duan, J.; Chen, Z. Enhanced pseudocapacitive behaviors of Sb-based anodes for lithium ion batteries via dual modification approach of Fe doping combined with double carbon coatings. *J. Alloys Compd.* **2021**, *889*, 161658. [CrossRef]

24. Wu, Y.L.; Zhua, C.; Shu, L.; Duan, J.F.; Wei, D.H.; Xu, J.X.; Zhu, Z.Y.; Li, L.J.; Peng, Z.Y.; Chen, Z.Y. Co_9S_8 confined in bifunctional N/S co-doped carbon/carbon with high electrochemical performance for lithium-ion batteries. *Appl. Surf. Sci.* **2019**, *489*, 528–537. [CrossRef]

25. Yan, T.C.; Wen, F.; Duan, J.F.; Zhu, C.; Wen, J.H.; Wang, Y.X.; Tong, J.T.; Chen, Z.Y. Fabricating tunable metal sulfides embedded with honeycomb-structured N-doped carbon matrices for high-performance lithium-ion capacitors. *Chem. Eng. J.* **2023**, *474*, 145839–145850. [CrossRef]

26. Huang, G.; Hu, M.; Xu, X.T.; Alothman, A.A.; Mushab, M.S.S.; Ma, S.J.; Shen, P.K.; Zhu, J.L.; Yamauchi, Y. Optimizing Heterointerface of Co_2P-Co_xO_y Nanoparticles within a Porous Carbon Network for Deciphering Superior Water Splitting. *Small Struct.* **2023**, *4*, 2200235–2200244. [CrossRef]

27. Tan, L.; Huang, X.; Yin, T.; Guo, Y.; Ning, T.; Mei, Y.; Zou, K.; Li, L.; Ji, X.; Zou, G. A 5 V ultrahigh energy density lithium metal capacitor enabled by the fluorinated electrolyte. *Energy Storage Mater.* **2024**, *71*, 103692. [CrossRef]

28. Cheng, Q.; Liu, X.Z.; Deng, Q.; Chen, C.D.; Zhong, W.T.; Yang, C.H. Heterostructured Ni_3S_4/Co_9S_8 Encapsulated in Nitrogen-Doped Carbon Nanocubes for Advanced Potassium Storage. *Chem. Eng. J.* **2022**, *446*, 136829–136836. [CrossRef]

29. Zhang, J.F.; Sun, C.H.; Qu, S.Q.; Qian, M.M.; Zhan, W.; Su, A.Q.; Zhang, K.; Liu, Q.; Shao, R.W.; Wang, J.; et al. Paradigm metallothermic-sulfidation-carbonization constructing ZIFs-derived TMSs@Graphene/CNx heterostructures for high-capacity and long-life energy storage. *Nano Energy* **2023**, *111*, 108401–108410. [CrossRef]

30. Shen, M.; Ma, H. Metal-organic frameworks (MOFs) and their derivative as electrode materials for lithium-ion batteries, Coordination. *Chem. Rev.* **2022**, *470*, 214715.

31. Shi, X.; Li, G.; Liu, X.; Li, J.; Zhang, X.; Guo, J. Carbon coated $Co(PO_3)_2$/$CoSe_2$ heterostructure as high performance sodium storage anode. *J. Alloys Compd.* **2023**, *951*, 169989. [CrossRef]

32. Zhong, H.Y.; Lu, X.; Zhong, Y.; Zhao, Y.; Liu, X.M.; Cheng, D.H.; Huang, X.Y.; Du, K.Z.; Wu, X.H. Lithium Storage Performance Boosted via Delocalizing Charge in $Zn_xCo_{1-x}PS_3$/CoS_2 of 2D/3D Heterostructure. *Small* **2022**, *18*, 2104295. [CrossRef]

33. Cheng, W.; Di, H.F.; Shi, Z.; Zhang, D. Synthesis of ZnS/CoS/CoS_2@N-doped carbon nanoparticles derived from metal-organic frameworks via spray pyrolysis as anode for lithium-ion battery. *J. Alloys Compd.* **2020**, *831*, 154607. [CrossRef]

34. Li, Q.; Xu, M.Q.; Wang, T.; Wang, H.J.; Sun, J.W.; Sha, J.Q. Nanohybridization of CoS_2/MoS_2 Heterostructure with Polyoxometalate on Functionalized Reduced Graphene Oxide for High-Performance LIBs. *Chem. A Eur. J.* **2022**, *28*, e202200207. [CrossRef] [PubMed]

35. Nong, Y.T.; Zhang, M.; Li, Q.Q.; Pan, Q.C.; Huang, Y.G.; Wang, H.Q.; Zheng, F.H.; Li, Q.Y. Carbon coated bimetallic sulfides Co_9S_8/ZnS heterostructures microrods as advanced anode materials for lithium ion batteries. *J. Taiwan Inst. Chem. Eng.* **2022**, *141*, 104601. [CrossRef]

36. Zhu, L.; Lu, H.Y.; Xiao, F.P.; Yao, T.H.; Liu, T.; Li, F.; Wang, J.K.; Han, X.G.; Cheng, Y.H.; Wang, H.K. Flower-like Mn/Co Glycerolate-Derived α-MnS/Co$_9$S$_8$/Carbon Heterostructures for High-Performance Lithium-Ion Batteries. *ACS Appl. Energy Mater.* **2020**, *3*, 10215. [CrossRef]

37. Hou, J.B.; Shao, Y.Y.; Ellis, M.W.; Moore, R.B.; Yi, B.L. Graphene-based electrochemical energy conversion and storage: Fuel cells, supercapacitors and lithium ion batteries. *Phys. Chem. Chem. Phys.* **2011**, *13*, 15384–15402. [CrossRef]

38. Tao, S.S.; Momen, R.; Luo, Z.; Zhu, Y.R.; Xiao, X.H.; Cao, Z.W.; Xiong, D.Y.; Deng, W.T.; Liu, Y.C.; Hou, H.S.; et al. Trapping Lithium Selenides with Evolving Heterogeneous Interfaces for High-Power Lithium-Ion Capacitors. *Small* **2023**, *19*, 2207975. [CrossRef]

39. Shi, Z.C.; Wei, S.; Zuo, H.; Huang, M.H.; Shi, J.; Wang, H.L. Boosting capacitance and energy density by construction NiCoO$_2$/CoS$_2$ nanocomposites arrays as pseudocapacitor. *J. Alloys Compd.* **2021**, *881*, 160627. [CrossRef]

40. Wang, S.Q.; Song, Y.P.; Ma, Y.; Zhu, Z.Q.; Zhao, C.H.; Zhao, C.J. Attaining a high energy density of 106 Wh kg^{-1} for aqueous supercapacitor based on VS$_4$/rGO/CoS$_2$@Co electrode. *Chem. Eng. J.* **2019**, *365*, 88. [CrossRef]

41. Sonia, Y.K.; Paliwal, M.K.; Meher, S.K. The rational design of hierarchical CoS$_2$/CuCo$_2$S$_4$ for three-dimensional all-solid-state hybrid supercapacitors with high energy density, rate efficiency, and operational stability. *Sustain. Energy Energy Fuels* **2021**, *5*, 973. [CrossRef]

42. Li, X.N.; Zhang, W.Y.; Kang, H.W.; Liu, H.L.; Yang, B.C.; Li, Z.J.; Li, Z.K. Self-assembled CoS$_2$/NiCo$_2$S$_4$/RGO nanohybrids as advanced electrode for hybrid supercapacitor with enhanced energy density and ultra-long durability. *J. Energy Storage* **2023**, *67*, 107528. [CrossRef]

43. Wang, Y.K.; Liu, M.C.; Cao, J.Y.; Zhang, H.J.; Kong, L.B.; Trudgeon, D.P.; Li, X.H.; Frank, C.W. 3D Hierarchically Structured CoS Nanosheets: Li+ Storage Mechanism and Application of the High-Performance Lithium-Ion Capacitors. *ACS Appl. Mater. Interfaces* **2020**, *12*, 3709. [CrossRef] [PubMed]

44. Wang, H.Y.; Tian, L.H.; Zhao, X.; Ali, M.; Feng, H.M.; Han, S.Y.; Xing, Z.C.; Kumar, S.; Ding, J. Synthesis of MoS$_2$/CoS composite electrode and its application for supercapacitors. *J. Alloys Compd.* **2023**, *960*, 170835. [CrossRef]

45. Reddy, P.A.K.; Han, H.; Kim, K.C.; Bae, S. Synthesis of ZIF-67-derived CoS$_2$@graphitic carbon/reduced graphene oxide for supercapacitor application. *Chem. Eng. J.* **2023**, *471*, 144608. [CrossRef]

46. Zhang, K.; Gao, X.; Yao, F.; Xie, Y.Q.; Bai, H.; Sun, Y.J.; Liu, R.R.; Yue, H.Y. Construction of hierarchical MOF-derived CoS$_2$ microsheet arrays@NiMo$_2$S$_4$ nanoflakes on Ni foam as a high-performance supercapacitor electrode. *J. Colloid Interface Sci.* **2023**, *650*, 105. [CrossRef]